Biomaterials Science

ROYAL SOCIETY OF CHEMISTRY

PAPER

View Article Online
View Journal | View Issue

Cite this: *Biomater. Sci.*, 2021, **9**, 3069

Sequential SPECT and NIR-II imaging of tumor and sentinel lymph node metastasis for diagnosis and image-guided surgery†

Xiaolu Zhang,‡[a,b] Meng Zhao,‡[b] Ling Wen,‡[c] Manran Wu,[b] Yi Yang,[b] Yujuan Zhang,[d] Yan Wu,[b] Jian Zhong,*[a] Haibin Shi,[b] Jianfeng Zeng,[b] Guanglin Wang*[b] and Mingyuan Gao*[b]

Efficacious cancer treatment largely relies on accurate imaging diagnosis and imaging-guided surgery, which can be achieved by combining different mode imaging probes on one single nanoplatform. Herein, a novel radiolabeled NIR-II nanoprobe (^{125}I-MT NP) was developed to enable versatile single-photon emission computed tomography (SPECT) and second near-infrared (NIR-II) fluorescence dual-modal imaging against breast cancer. ^{125}I-MT was precipitated with an amphiphilic triblock copolymer (PEO-PPO-PEO) to form ^{125}I-MT NPs. The ^{125}I-MT NPs exhibited high labeling efficiency (98 ± 2%) with a hydrodynamic diameter of 91.3 ± 5.5 nm. *In vitro* and *in vivo* studies demonstrated that ^{125}I-MT NPs emitted intensive NIR-II fluorescence and SPECT signals, and possessed good biocompatibility. By using a breast tumor xenograft mouse model after intravenous injection of ^{125}I-MT NPs, the SPECT imaging and NIR-II imaging showed clear images of tumor tissues at 8 h and 48 h postinjection, respectively, suggesting the feasibility of using ^{125}I-MT NPs to detect tumors before surgery and visualize the dissection area during surgery. In addition, the SPECT scan of a lymph node mapping was performed at 1 h postinjection and NIR-II fluorescence imaging was carried out at 4 h postinjection. This further guarantees the accurate imaging of lymph nodes before and during surgery for lymphadenectomy. Overall ^{125}I-MT NP is a promising, practical imaging probe for sequential imaging and precision cancer therapy.

Received 18th January 2021,
Accepted 13th February 2021

DOI: 10.1039/d1bm00088h

rsc.li/biomaterials-science

Introduction

In clinical practice, imaging of tumor tissues is often carried out to locate and monitor tumors as a diagnostic tool and for imaging-guided surgery (*i.e.*, surgical resection of the primary tumor and metastatic tissues).[1,2] To improve the surgical accuracy, dual-modal and multimodal imaging have been successfully employed for tumor diagnosis and imaging-guided surgery. A combination of nuclear imaging and optical imaging integrating the advantages of high sensitivity and real-time imaging has attracted considerable interest.[3–6] Nuclear imaging, such as single photon emission computed tomography (SPECT), is a widely applied clinical noninvasive functional imaging technique that uses a radionuclide-labeled probe to specifically target tumor and tissue for diagnosis with unlimited penetration, high sensitivity, and precise quantification.[7] Optical imaging, also called fluorescence imaging, is commonly performed in the visible and near-infrared wavelengths (~400–1700 nm) for simplicity and real-time imaging.[8] A combination of SPECT and fluorescence imaging overcomes the limited spatial resolution and long scan time of SPECT in surgery, as well as the non-quantitative capability and short penetration of fluorescence in diagnosis.[9,10] More importantly, dual modality contrast agents can ensure that the signals obtained from each modality are collected from the same contrast agent, realizing the cross-validation of each imaging modal.[11–15]

[a]*Integrated Scientific Research Base on Comprehensive Utilization Technology for By-Products of Aquatic Product Processing, Ministry of Agriculture and Rural Affairs of the People's Republic of China, National R&D Branch Center for Freshwater Aquatic Products Processing Technology (Shanghai), Shanghai Engineering Research Center of Aquatic-Product Processing and Preservation, College of Food Science & Technology, Shanghai Ocean University, Shanghai, 201306, China. E-mail: jzhong@shou.edu.cn*

[b]*State Key Laboratory of Radiation Medicine and Protection, School of Radiation Medicine and Protection & School for Radiological and Interdisciplinary Sciences (RAD-X), Collaborative Innovation Center of Radiation Medicine of Jiangsu Higher Education Institutions, Soochow University, Suzhou 215123, PR China. E-mail: glwang@suda.edu.cn, gaomy@iccas.ac.cn*

[c]*Department of Radiology, the First Affiliated Hospital of Soochow University, Institute of Medical Imaging, Soochow University, Suzhou 215000, PR China*

[d]*Experimental Center of Soochow University, Department of Medicine, Soochow University, Suzhou 215123, PR China*

†Electronic supplementary information (ESI) available. See DOI: 10.1039/d1bm00088h

‡These authors contributed equally.

A simple combination of fluorescent dye and radionuclides could not effectively target tumor sites, thus a carrier or targeting agent is generally required, for example, peptides, antibodies and nanocarriers.[16–21] However, a small molecular dye can commonly be excreted rapidly due to its short blood circulation time, which is not desirable for efficient tumor targeting and prolonged imaging. Antibodies have very good specificity for a certain kind of tumor, but for tumor diagnosis, especially early diagnosis, it is very important to have probes that can diagnose a variety of tumors. Nanocarriers can accumulate in tumors through an enhanced and permeation retention effect, and are suitable for tumor diagnosis, especially early diagnosis. To date, the most often reported fluorescent dye was the first near-infrared fluorescent (NIR-I) dye which emits from 650 nm to900 nm with several millimeter penetration depth, such as indocyanine green (ICG), that has been approved by the Food and Drug Administration (FDA) for clinical applications.[22] Compared to NIR-I fluorescence imaging, second near-infrared (NIR-II) fluorescence imaging (900–1700 nm) has attracted enormous attention, due to the high spatio-temporal resolution, decrease of photon scattering, negligible tissue autofluorescence, and deep tissue penetration.[23–30] These features could provide a novel platform for image-guided surgery. However, so far, most reported SPECT/NIR dual probes are radionuclides combined with NIR-I dye.

Furthermore, according to the time and aims of using imaging technologies for surgery, medical imaging includes preoperative, intraoperative, and postoperative imaging.[31] For preoperative imaging, noninvasive and deep penetration is required, while a high spatio-temporal resolution is required for intraoperative imaging. Different agents have been used for each step of imaging without a combination of preoperative and intraoperative imaging. To achieve the same diagnostic capability, it is better to develop an agent that is useful for both preoperative and intraoperative imaging with two imaging windows.

It is well known that aggregation-caused quenching is a major cause of weak emission for hydrophobic fluorescent dyes at high concentrations.[32] Hence, the fluorescence of a hydrophobic fluorescent dye encapsulated into polymeric nanoparticles could be turned on after decomposition. In this work, we designed a facile nanoengineering approach to construct a nanoprobe (^{125}I-MT NP) that was fabricated by encapsulating a radiolabeled hydrophobic NIR-II dye (^{125}I-MT) into an amphiphilic block copolymer, realizing dual modality imaging including SPECT and NIR-II fluorescence imaging. The SPECT and NIR-II imaging capability of ^{125}I-MT NPs were demonstrated with a subcutaneous tumor and lymph node metastatic tumor *in vivo*. The maximum accumulation of subcutaneous tumor was found at 8 h postinjection from SPECT imaging but at 48 h postinjection from NIR-II imaging. In general, different imaging time windows of SPECT and NIR-II fluorescence imaging provide dual modality and sequential imaging opportunity for diagnosis and image-guided surgery as shown in Scheme 1.

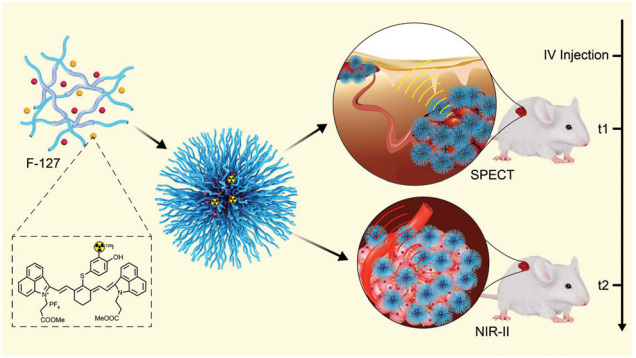

Scheme 1 A schematic illustration shows the preparation of ^{125}I-MT NPs with SPECT and NIR-II sequential imaging of cancer.

Results and discussion

Preparation and characterization of MT nanoparticles (MT NPs) and ^{125}I-MT nanoparticles (^{125}I-MT NPs)

The preparation of water-soluble ^{125}I-MT NPs involved three main steps: the synthesis of a hydrophobic small-molecular dye (MT) which emits NIR-II fluorescence and provides a functional group for radiolabeling, ^{125}I-labeling of MT, and the nanoprecipitation of ^{125}I-MT with an amphiphilic block copolymer poly(ethylene glycol)-*b*-poly(propylene glycol)-poly(ethylene glycol) (PEO-PPO-PEO). First, MT was synthesized *via* a nucleophilic substitution reaction using NIR-II dye (compound 4) and 4-mercaptophenol in *N*,*N*-dimethylformamide solution according to our previously reported protocol,[33,34] as shown in Scheme S1.† Second, using the chloramine-T oxidation method, MT dissolved in DMSO was radiolabeled with ^{125}I at the *ortho*-position of the phenol group at room temperature. The radiolabeling efficiency of ^{125}I-MT reached 98 ± 2% as quantified by thin layer chromatography (Fig. S1†). The radiostability of ^{125}I-MT was analyzed in PBS and 10% FBS by TLC. As shown in Fig. S2,† less than 6% of free ^{125}I was found in the solution within 4 h and then no free ^{125}I was found up to 96 h, indicating that ^{125}I-MT was very stable. Finally, an amphiphilic triblock copolymer PEO-PPO-PEO was used to transform hydrophobic ^{125}I-MT into water-soluble nanoparticles. The radiolabeling efficiency of ^{125}I-MT NPs was 73 ± 2%. The non-radioactive nanoparticles (MT NPs) were prepared by the same method using MT instead of ^{125}I-MT. The transmission electron microscopy (TEM) image revealed the spherical morphology of MT NPs with an average diameter of 42 ± 10 nm (Fig. 1a). The average hydrodynamic diameter of MT NPs was found to be 91.3 ± 5.5 nm with a polydispersity index (PDI) of 0.12 by dynamic light scattering (DLS) (Fig. 1a). Moreover, the stability of MT NPs was measured by DLS up to 96 h; the results show a variation of the diameter and the PDI was in the error range, and no obvious sediment was observed during storage, indicating excellent stability of the MT NPs (Fig. 1b).

To assess the optical properties, the absorption and fluorescence spectra of MT and MT NPs in PBS were recorded on a UV-vis-NIR and fluorescence spectrometer (FLS908), respect-

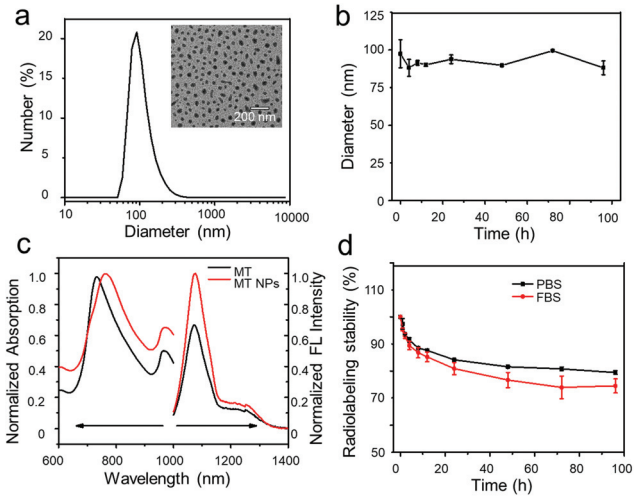

Fig. 1 (a) Diameter and morphology of MT NPs were characterized by DLS and TEM. (b) Colloid stability of MT NPs in PBS. (c) UV absorbance spectra of MT and MT NPs and NIR-II fluorescence emission spectra of MT and MT NPs. (d) Radiostability of ^{125}I-MT NPs in PBS and 10% FBS.

ively. MT NPs exhibited a maximum absorption peak at 760 ± 3 nm, which was at 730 ± 3 nm for MT. Such a slight red-shift for MT NPs was probably caused by the aggregation of MT within the nanoparticles. Similarly, MT NPs had an emission peak at 1076 ± 3 nm compared to that for at 1072 ± 2 nm, confirming that MT NPs can act as excellent contrast agents for NIR-II fluorescence imaging (Fig. 1c). Furthermore, the optical stability of MT-NPs was evaluated in PBS over time. The results showed that the UV absorption changed from 0.52 at 0 h to 0.41 at 48 h, which could be induced by the leakage of MT from MT NPs (Fig. S3†).

To evaluate the radiostability of ^{125}I-MT NPs in different solutions, the prepared dispersion was dialyzed in the phosphate buffer solution (PBS) and 10% fetal bovine serum (FBS) over time. The detected activity signals of ^{125}I in the buffer increased within the first 24 h and reached a plateau at 96 h, confirming that 20% and 25% of the incorporated ^{125}I-MT slowly leaked from ^{125}I-MT NPs in PBS and 10% FBS, respectively (Fig. 1d). We further tested the radiostability of 10 times diluted ^{125}I-MT NPs in PBS and 10% serum. The results showed that a similar loss was found at 96 h (Fig. S4†). According to the literature, the loaded hydrophobic agent was slowly released from the polymeric nanoparticles especially without crosslinking of the polymeric nanoparticles, likely owing to the dissociation of nanoparticles, caused by the weak interaction between the agent and nanoparticle core, and the unstable encapsulation of the agent.[35–37]

In order to investigate the NIR-II fluorescence imaging capability of MT NPs, the phantom water, MT in H_2O, MT NPs in H_2O, MT in 10% FBS, MT NPs in 10% FBS, and MT in DMSO with the same concentration of 3×10^{-5} μmol mL^{-1} were imaged on an NIR-II imaging system. The results showed that MT in DMSO was brilliantly bright, while MT in 10% FBS and MT-NPs in 10% FBS were bright. In contrast, the fluorescence signal of MT or MT NPs in PBS was not observed (Fig. S5a†). Generally, hydrophobic dyes aggregate in poor solvents and cause quenching.[38] As shown in Fig. S5b,† quantification of the NIR-II images of phantom showed that the fluorescence intensity increased with increasing the mixing time of MT in 10% FBS and MT NPs in 10% FBS. The strong emission of cyanine dyes in serum has been attributed to the interaction between the fluorescent dyes and the hydrophobic segment of plasma proteins.[39,40]

Cytotoxicity

To investigate the biosafety of the resultant nanoprobes, the cytotoxicity of MT, MT NPs and ^{125}I-MT NPs was evaluated with 4T1 tumor cells by the methyl thiazolyl tetrazolium (MTT) assay. It was found that no obvious toxicity was observed for MT NPs even at a concentration of 52.5 μg mL^{-1} while MT remarkably decreased the viability of 4T1 cells under the same conditions (Fig. 2a). Similarly, ^{125}I-MT NPs also exhibited no obvious toxicity to 4T1 cells at a radioactivity of 10 μCi (corresponding to 6.56 μg mL^{-1} of MT NPs) (Fig. 2b). Notably, the overdose of ^{125}I potentially induced radiotoxicity due to the damage of DNA by Auger electrons emitted from ^{125}I.[41,42] Furthermore, the radiotoxicity of ^{125}I-MT NPs was examined by the immunofluorescence assay and no DNA double strand breaks were found, further validating that no radiotoxicity of ^{125}I-MT NPs was observed at a dose of 10 μCi (Fig. S6†). Moreover, the cytotoxicity was tested by colony formation of 4T1 cells. The results indicated that the colony formation of ^{125}I-MT NPs was similar to that of the control group (Fig. S7†).

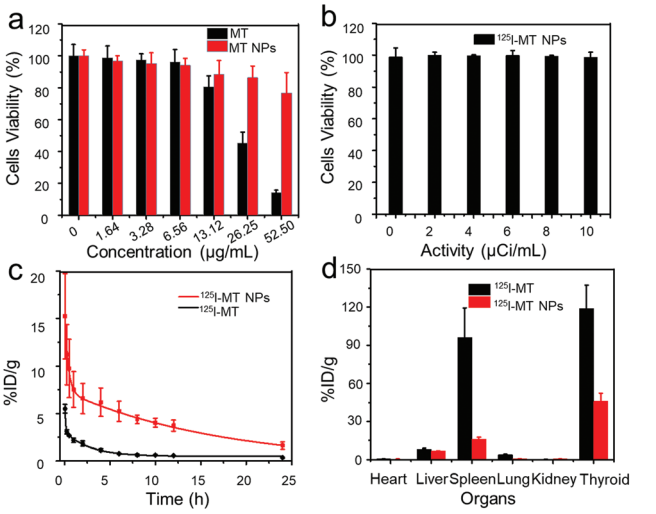

Fig. 2 (a) Cell viability of MT and MT NPs at MT concentrations of 0 to 52.50 μg mL^{-1} in 4T1 cells during 24 h incubation (n = 6). (b) MTT assays of ^{125}I-MT at activities varying from 0 to 10 μCi mL^{-1} in 4T1 cells following 24 h incubation (n = 6). (c) The pharmacokinetics of ^{125}I-MT and ^{125}I-MT NPs in mice following intravenous injection (n = 3). (d) The biodistribution of ^{125}I-MT and ^{125}I-MT NPs in mice at 24 h post injection (n = 3).

The above results demonstrated that ^{125}I-MT NPs have good biosafety for further *in vivo* study.

Pharmacokinetics and biodistribution

To assess the pharmacokinetics and biodistribution of ^{125}I-MT NPs, the *in vivo* behavior of ^{125}I-MT NPs was examined in BABL/C mice. The mice were intravenously injected with ^{125}I-MT and ^{125}I-MT NPs at a dose of 30 μCi (corresponding to 2.22×10^{-4} mmol mL^{-1} of MT, 50 μL). The blood sample was collected from the retinal vein for radioactivity measurement at different postinjection times. The blood circulation of nanoparticles could be fitted by a two-compartment body model. ^{125}I-MT NPs had a biodistribution half-life of 0.21 h ($t_{1/2\alpha}$) and an elimination half-life of 10.5 h, which were remarkably prolonged compared with those of ^{125}I-MT that had a distribution half-life and elimination half-life of 0.079 h and 4.1 h, respectively (Fig. 2c). At 24 h postinjection, the major organs collected from the injected mice were weighed and the radioactivity was also measured by a gamma counter. It was found that the percentage of injected dose per gram tissue (%ID g^{-1}) of ^{125}I-MT NPs exhibited higher accumulation in the spleen (16.12 ± 1.58 %ID g^{-1}) than that in the liver (6.80 ± 0.22 %ID g^{-1}). However, ^{125}I-MT exhibited much higher accumulation in the spleen (96.18 ± 23 %ID g^{-1}) which was 6-fold that of ^{125}I-MT NPs. It should be noted that the higher activity in the thyroid is due to the function of the thyroid and absorption of free radioactive iodine. In clinical practice, patients can be administered non-radioactive iodine to decrease the absorption of radioactive iodine (Fig. 2d).

In addition, SPECT was used to monitor the biodistribution of ^{125}I-MT (5×10^{-4} mmol mL^{-1}, 250 μCi) and ^{125}I-MT NPs (5×10^{-4} mmol mL^{-1}, 250 μCi) over time up to one week in healthy mice after intravenous injection. The resulting maximum intensity projection (MIP) images demonstrated that both ^{125}I-MT NPs and ^{125}I-MT were mainly accumulated in the liver and spleen up to the 7th day. However, the accumulation of ^{125}I-MT was much higher than that of ^{125}I-MT NPs in the spleen (Fig. S8a†). The radioactivity in mice postinjection was measured by a dosimeter. As shown in Fig. S8b,† the radioactivity in mice with ^{125}I-MT NPs or ^{125}I-MT treatment was decreased rapidly from 100% to 36.48 ± 1.90% and 27.81 ± 2.60%, respectively, at 24 h post injection. The remaining radioactivities of ^{125}I-MT NPs and ^{125}I-MT were 16.26 ± 0.61% ID and 27.81 ± 2.60%ID at 7 days post injection. Rapid excretion is a prerequisite of an ideal imaging contrast agent after it exerts the function.[43] At the 7th day, the biodistribution of ^{125}I-MT NPs and ^{125}I-MT was mainly concentrated in the liver and spleen and the distribution of ^{125}MT was higher than that of ^{125}I-MT NPs (43.81 ± 6.95 %ID g^{-1} *vs.* 14.59 ± 2.13 %ID g^{-1}) (Fig. S8c†). Therefore, the SPECT data were in agreement with the biodistribution data.

Next, we evaluated the potential toxicity of MT and MT NPs (150 μCi) after intravenous injection. After 7 days, the major organs were harvested and stained. As shown in Fig. S9,† hematoxylin and eosin (H&E) staining showed that no obvious toxicity was observed in the major organs, indicating that MT NPs are safe for further *in vivo* study.

In vivo NIR-II fluorescence and SPECT imaging

In order to explore the dual-modal imaging capability, 4T1 subcutaneous tumor-bearing BALB/c mice were intravenously injected with MT NPs (5×10^{-4} mol mL^{-1}, 200 μL) and ^{125}I-MT NPs (150 μCi, 5×10^{-4} mol mL^{-1}, 200 μL) for NIR-II fluorescence and SPECT imaging, respectively. As shown in Fig. 3a, the NIR-II fluorescence images of mice with MT NP treatment indicated that the fluorescence signal of MT could delineate the tumor at 24 h postinjection and became brilliantly bright from 48 h postinjection to 96 h postinjection. The NIR-II fluorescence intensities of MT NPs in tumors increased from 1.57×10^4 at 1 h to 3.95×10^4 at 48 h, and then gradually decreased to 3.0×10^4 at 96 h (Fig. 3b), which provides enough time for surgery. However, the obtained SPECT images showed an obvious accumulation of ^{125}I-MT NPs in the tumor immediately after intravenous injection, and reached a plateau at 8 h postinjection (Fig. 3a). Quantifying the volume of interest from the SPECT images of tumor uptake, the percentage of injected dose per gram of tumor tissues was quickly increased to 1.8 ± 0.16 %ID g^{-1} at 4 h postinjection and leveled off as a plateau at 2.0 ± 0.16 %ID g^{-1} until 96 h, as shown in Fig. 3c.

Compared with MT NPs and ^{125}I-MT NPs, no obvious tumor uptake of MT or ^{125}I-MT was found both in NIR-II and SPECT imaging at 96 h post injection as shown in Fig. 3a. Generally, nanoparticles accumulate in tumor tissues within several hours *via* the enhanced permeation and retention (EPR) effect.[44,45] Furthermore, compared with the tumor uptake between SPECT and NIR-II images, it was found that the signal of SPECT presented earlier than the signal of NIR-II. To normalize the tumor uptake, the presented signal of SPECT was found at 4 h postinjection from SPECT images while the fluorescence signal was found at 24 h postinjection from NIR-II images as shown in Fig. 3d. It is well known that SPECT imaging detected the γ rays directly emitted from radionuclides and is hardly influenced by the tumor microenvironment, while the emission of a fluorescent dye is strongly affected by the surrounding physical properties.[39] The fluorescence intensity differs drastically in different solvents. As shown in phantom studies (Fig. S5a†), MT NPs emitted brilliantly bright fluorescence in 10% FBS. Hence, SPECT could directly detect the radionuclide signals. NIR-II imaging could detect the fluorescence signals when the fluorescence dye was released from the nanoparticles and interacted with the protein. The mechanism of two imaging techniques offers the possibility of sequential imaging. Besides, the two scan windows providing the potential sequential imaging when using short half-life radionuclides will limit the radiation exposure to the surgical staff during the surgery.

Lymphatic metastasis is one of the main leading pathways that cause tumor metastasis and poor prognosis,[46] which underscores the compelling need for mapping of lymphatic metastasis.[47,48] A lymph node metastatic model was estab-

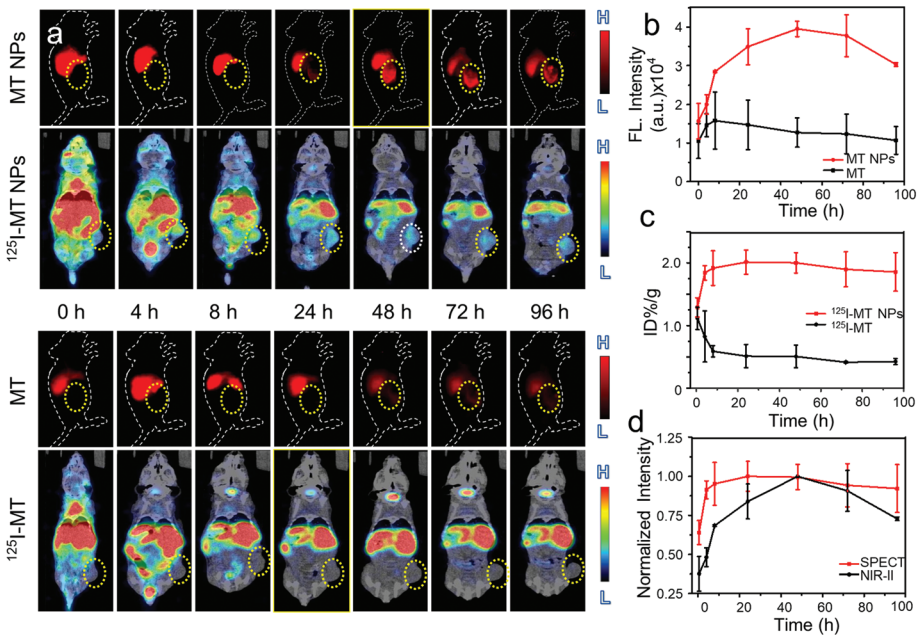

Fig. 3 (a) *In vivo* NIR-II and SPECT dual modality imaging of subcutaneous 4T1 tumor-bearing BALB/c mice at 0, 4, 8, 24, 48, 72 and 96 h postinjection of MT NPs and ^{125}I-MT NPs. Tumor uptake quantification of MT NPs and ^{125}I-MT NPs by NIR-II (b) and SPECT images (c). Normalized tumor uptake of MT NPs and ^{125}I-MT NPs by NIR-II and SPECT images (d). The yellow dotted circles show the 4T1 tumor.

lished by inoculating 4T1 tumor cells into footpads of 6–8 week old BALB/c mice. After four weeks, the H&E staining proved that the 4T1 cells had metastasized to the lymph node as shown in Fig. S10.† To evaluate the dual modality imaging capability in lymph node mapping, the probe was administered at a dose of 2.22×10^{-4} mmol mL^{-1} (30 μCi, 50 μL) *via* intratumoral injection, and imaged by the NIR-II system and SPECT. The NIR-II imaging showed that the MT NP signals were observed at 1 h postinjection, whereas the ^{125}I-MT NP signals from the SPECT imaging were observed immediately in

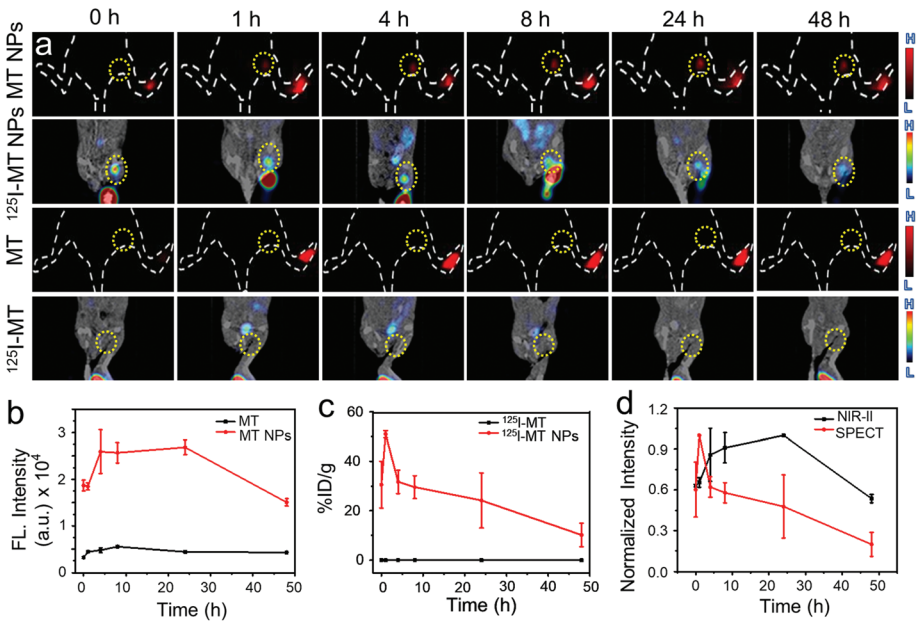

Fig. 4 (a) *In vivo* NIR-II and SPECT dual modality imaging of lymphatic metastasis 4T1 tumor-bearing BALB/c mice at 0, 4, 8, 24, 48, 72 and 96 h postinjection of MT NPs and ^{125}I-MT NPs. Tumor uptake quantification of MT NPs and ^{125}I-MT NPs by NIR-II (b) and SPECT images (c). Normalized tumor uptake of MT NPs and ^{125}I-MT NPs by NIR-II and SPECT images (d). The yellow dotted circles show the sentinel lymph node.

the lymphatic metastasis tumor after intratumoral injection. However, no lymph node uptake of MT and ^{125}I-MT was found even at 48 h after injection as shown in Fig. 4a. To further quantify the lymph metastasis, the fluorescence intensity of MT NPs in the lymph node was found to be 1.84×10^4 at 1 h and then increased from 2.59×10^4 at 4 h to 2.69×10^4 at 24 h postinjection (Fig. 4b). Meanwhile, from the quantification of SPECT images, the lymphatic metastasis uptake of ^{125}I-MT NPs was above 10 %ID g^{-1} after injection until 48 h and achieved a maximum of 50.99 ± 1.42 %ID g^{-1} at 1 h postinjection (Fig. 4b). However, the uptake of ^{125}I-MT in the lymphatic metastasis was less than 1 %ID g^{-1}.

By normalizing the intensity of NIR-II and SPECT signals, we found that the radio-signal from SPECT images was observed in the lymph node immediately after injection and reached a maximum at 1 h, while the fluorescence signal from NIR-II images was observed at 1 h and then reached a maximum at 4 h after injection (Fig. 4d). The signal of MT NPs presented in the lymph node tumor was much shorter than that in the subcutaneous tumor model, which could be explained by the fact that the absolute amount of dye that leaked from the nanoparticles is higher in the lymph node tumor. From the quantification analysis, the percentage injection dose of lymph node tumor uptake was much higher than that of the subcutaneous tumor model. The above results showed that ^{125}I-MT NPs could be used as a lymph node contrast agent for sequential imaging with faster accumulation and higher lymph node tumor uptake.

Conclusions

In summary, we have demonstrated that ^{125}I-MT NPs can be used for SPECT and NIR-II dual modality imaging with two scan windows for diagnosis and image-guided surgery. ^{125}I-MT NPs were uniform nanoparticles in aqueous solution of one hundred nanometers in size. *In vitro* and *in vivo* studies showed that the probe possessed good biosafety. The SPECT scan of a subcutaneous tumor modal could be performed at 8 h postinjection while NIR-II fluorescence imaging could be carried out 48 h postinjection. In addition, the SPECT scan of lymph node mapping could be performed at 1 h postinjection and NIR-II fluorescence imaging could be carried out at 4 h postinjection. ^{125}I-MT NPs provide high potential sequential imaging with two scan windows for diagnosis and image-guided surgery.

Ethical statement

All animal experiments were approved by the Animal Care and Use Committee of Soochow University (P. R. China), and all protocols of animal studies conformed to the Guide for the Care and Use of Laboratory Animals of Soochow University (P. R. China).

Author contribution

The manuscript was written through contributions of all authors. All authors have given approval to the final version of the manuscript.

Conflicts of interest

The authors declare no competing financial interest.

Acknowledgements

The authors are thankful for the financial support from the National Key Research and Science Foundation of China (2018YFA0208800), the National Natural Science Foundation of China (81720108024, 21976128, and 81701728), and the Priority Academic Program Development of Jiangsu Higher Education Institutions (PAPD). G. W. is thankful for the support from the Natural Science Foundation of Jiangsu Province (BK20160307 and BK20200100), the China Postdoctoral Science Foundation (2016M591915, 2018T110547), and the Suzhou Administration of Science & Technology (SYS201701). The authors thank Dr Sophia Zi Gu for her suggestions and valuable discussion.

References

1 T. Hussain and Q. T. Nguyen, *Adv. Drug Delivery Rev.*, 2014, **66**, 90–100.
2 V. Ntziachristos, J. Ripoll, L. h. V. Wang and R. Weissleder, *Nat. Biotechnol.*, 2005, **23**, 313–320.
3 M. F. Kircher, H. Hricak and S. M. Larson, *Mol. Oncol.*, 2012, **6**, 182–195.
4 J. X. Ge, Q. Y. Zhang, J. F. Zeng, Z. Gu and M. Y. Gao, *Biomaterials*, 2020, **228**, 119553.
5 J. Kim, Y. Z. Piao and T. Hyeon, *Chem. Soc. Rev.*, 2009, **38**, 372–390.
6 D. W. Jiang, Y. L. Sun, J. Li, Q. Li, M. Lv, B. Zhu, T. Tian, D. F. Cheng, J. Y. Xia, L. Zhang, L. H. Wang, Q. Huang, J. Y. Shi and C. H. Fan, *ACS Appl. Mater. Interfaces*, 2016, **8**, 4378–4384.
7 J. Culver, W. Akers and S. Achilefu, *J. Nucl. Med.*, 2008, **49**, 169–172.
8 Q. Li, S. H. Li, S. S. He, W. Chen, P. H. Cheng, Y. Zhang, Q. Q. Miao and K. Y. Pu, *Angew. Chem., Int. Ed.*, 2020, **59**, 7018–7023.
9 F. W. B. van Leeuwen, M. Schottelius, O. R. Brouwer, S. Vidal-Sicart, S. Achilefu, J. Klode, H.-J. Wester and T. Buckle, *J. Nucl. Med.*, 2020, **61**, 13–19.
10 T. Buckle, D. M. van Willigen, S. J. Spa, A. W. Hensbergen, S. van der Wal, C. M. de Korne, M. M. Welling, H. G. van der Poel, J. C. H. Hardwick and F. W. B. van Leeuwen, *J. Nucl. Med.*, 2018, **59**, 986–992.

11 L. E. Jennings and N. J. Long, *Chem. Commun.*, 2009, 3511–3524.
12 M. Elsabahy, G. S. Heo, S. M. Lim, G. R. Sun and K. L. Wooley, *Chem. Rev.*, 2015, **115**, 10967–11011.
13 X. Y. Xu, L. Z. Zhao, X. Li, P. Wang, J. H. Zhao, X. Y. Shi and M. W. Shen, *Biomater. Sci.*, 2017, **5**, 2393–2397.
14 B. R. Smith and S. S. Gambhir, *Chem. Rev.*, 2017, **117**, 901–986.
15 X. W. Lin, C. B. Liu, Z. H. Sheng, X. J. Gong, L. Song, R. F. Zhang, H. R. Zheng and M. J. Sun, *ACS Appl. Mater. Interfaces*, 2018, **10**, 26064–26074.
16 B. Jia, X. Zhang, B. Wang, M. H. Chen, F. Y. Lv, S. Wang and F. Wang, *ACS Appl. Mater. Interfaces*, 2018, **10**, 6646–6651.
17 T. Kanagasundaram, C. S. Kramer, E. Boros and K. Kopka, *Dalton Trans.*, 2020, **49**, 7294–7298.
18 R. Yan, E. El-Emir, V. Rajkumar, M. Robson, A. P. Jathoul, R. B. Pedley and E. Arstad, *Angew. Chem., Int. Ed.*, 2011, **50**, 6793–6795.
19 R. Yan, K. Sander, E. Galante, V. Rajkumar, A. Badar, M. Robson, E. El-Emir, M. F. Lythgoe, R. B. Pedley and E. Årstad, *J. Am. Chem. Soc.*, 2013, **135**, 703–709.
20 B. T. Luk and L. F. Zhang, *ACS Appl. Mater. Interfaces*, 2014, **6**, 21859–21873.
21 M. Morais, M. P. C. Campello, C. Xavier, J. Heemskerk, J. D. G. Correia, T. Lahoutte, V. Caveliers, S. Hernot and I. Santos, *Bioconjugate Chem.*, 2014, **25**(11), 1963–1970.
22 J. A. Carr, D. Franke, J. R. Caram, C. F. Perkinson, M. Saif, V. Askoxylakis, M. Datta, D. Fukumura, R. K. Jain, M. G. Bawendi and O. T. Bruns, *Proc. Natl. Acad. Sci. U. S. A.*, 2018, **115**, 4465–4470.
23 C. Y. Li and Q. B. Wang, *ACS Nano*, 2018, **12**, 9654–9659.
24 A. L. Antaris, H. Chen, K. Cheng, Y. Sun, G. S. Hong, C. R. Qu, S. Diao, Z. X. Deng, X. M. Hu, B. Zhang, X. D. Zhang, O. K. Yaghi, Z. R. Alamparambil, X. C. Hong, Z. Cheng and H. J. Dai, *Nat. Mater.*, 2016, **15**, 235–242.
25 J. Y. Zhao, D. Zhong and S. B. Zhou, *J. Mater. Chem. B*, 2018, **6**, 349–365.
26 P. Y. Wang, Y. Fan, L. F. Lu, L. Liu, L. F. Fan, M. Y. Zhao, Y. Xie, C. J. Xu and F. Zhang, *Nat. Commun.*, 2018, **9**, 2898.
27 Y. Sun, M. M. Ding, X. D. Zeng, Y. L. Xiao, H. P. Wu, H. Zhou, B. B. Ding, C. R. Qu, W. Hou, A.GA. Er-bu, Y. J. Zhang, Z. Cheng and X. C. Hong, *Chem. Sci.*, 2017, **8**, 3489.
28 B. Guo, Z. H. Sheng, D. H. Hu, C. B. Liu, H. R. Zheng and B. Liu, *Adv. Mater.*, 2018, **30**, 1802591.
29 Q. Wang, Y. N. Dai, J. Z. Xu, J. Cai, X. R. Niu, L. Zhang, R. F. Chen, Q. M. Shen, W. Huang and Q. L. Fan, *Adv. Funct. Mater.*, 2019, **29**, 1901480.
30 F. Ding, Y. B. Zhan, X. J. Lu and Y. Sun, *Chem. Sci.*, 2018, **9**, 4370–4380.
31 C. Wang, W. P. Fan, Z. J. Zhang, Y. Wen, L. Xiong and X. Y. Cheng, *Adv. Mater.*, 2019, **31**, 1904329.
32 A. Reisch and A. S. Klymchenko, *Small*, 2016, **12**, 1968–1992.
33 M. Zhao, J. N. Ding, Q. L. Mao, Y. Q. Zhang, Y. J. Gao, S. Y. Ye, H. N. Qin and H. B. Shi, *Nanoscale*, 2020, **12**, 6953–6958.
34 L. Yin, H. Sun, H. Zhang, L. He, L. Qiu, J. G. Lin, H. W. Xia, Y. Q. Zhang, S. J. Ji, H. B. Shi and M. Y. Gao, *J. Am. Chem. Soc.*, 2019, **141**, 3265–3273.
35 Y. Q. Shen, Y. H. Zhan, J. B. Tang, P. S. Xu, P. A. Johnson, M. Radosz, E. A. Van Kirk and W. J. Murdoch, *AIChE J.*, 2008, **54**, 2979–2989.
36 M. L. Adams, A. Lavasanifar and G. S. Kwon, *J. Pharm. Sci.*, 2003, **92**, 1343–1355.
37 Q. H. Sun, Z. X. Zhou, N. S. Qiu and Y. Q. Shen, *Adv. Mater.*, 2017, **29**, 1606628.
38 E. D. Cosco, J. R. Caram, O. T. Bruns, D. Franke, R. A. Day, E. P. Farr, M. G. Bawendi and E. M. Sletten, *Angew. Chem., Int. Ed.*, 2017, **56**, 13126–13129.
39 B. H. Li, L. F. Lu, M. Y. Zhao, Z. H. Lei and F. Zhang, *Angew. Chem.*, 2018, **130**, 7605–7609.
40 A. L. Antaris, H. Chen, S. Diao, Z. R. Ma, Z. Zhang, S. J. Zhu, J. Wang, A. X. Lozano, Q. L. Fan, L. L. Chew, M. Zhu, K. Cheng, X. X. Hong, H. J. Dai and Z. Cheng, *Nat. Commun.*, 2017, **8**, 15269.
41 J. Grudzinski, I. Marsh, B. Titz, J. Jeffery, M. Longino, K. Kozak, K. Lange, J. Larrabee, A. Weichmann, A. Moser and B. Bednarz, *Cancer Biother.Radiopharm.*, 2018, **33**, 87–95.
42 A. Ku, V. J. Facca, Z. L. Cai and R. M. Reilly, *EJNMMI Radiopharm. Chem.*, 2019, **4**, 27.
43 S. S. He, J. C. Li, Y. Lyu, J. G. Huang and K. Y. Pu, *J. Am. Chem. Soc.*, 2020, **142**, 7075–7082.
44 V. P. Torchilin, *Pharm. Res.*, 2007, **24**, 1.
45 N. Brertrand, J. Wu, X. Y. Xu, N. Kamaly and O. C. Farokhzad, *Adv. Drug Delivery Rev.*, 2014, **66**, 2–25.
46 A. E. Giuliano, D. M. Kirgan, J. M. Guenther and D. L. Morton, *Ann. Surg.*, 1994, **220**, 391–401.
47 S. Kim, Y. Taik Lim, E. G. Soltesz, A. M. De Grand, J. Lee, A. Nakayama, J. A. Parker, T. Mihaljevic, R. G. Laurence, D. M. Dor, L. H. Cohn, M. G. Bawendi and J. V. Frangioni, *Nat. Biotechnol.*, 2004, **22**, 93–97.
48 Y. Sun, M. M. Yu, S. Liang, Y. J. Zhang, C. G. Li, T. T. Mou, W. J. Yang, X. Z. Zhang, B. Li, C. H. Huang and F. Y. Li, *Biomaterials*, 2011, **32**, 2999–3007.